

Finite Element Analysis of Adaptive-stiffening and Shape-control SMA Hybrid Composites

Xiujie Gao^{ab}, Deborah Burton^b, Travis L. Turner^c, and L. Catherine Brinson^{*bd}

^aCurrently at General Motors Research and Development, Warren, MI 48090

^bDepartment of Mechanical Engineering, Northwestern University, Evanston, IL 60208

^cNASA Langley Research Center, Structural Acoustics Branch, Mail Stop 463, Hampton, VA 23681

^dDepartment of Materials Science & Engineering, Northwestern University, Evanston, IL 60208

ABSTRACT

Shape memory alloy hybrid composites with adaptive-stiffening or morphing functions are simulated using finite element analysis. The composite structure is a laminated fiber-polymer composite beam with embedded SMA ribbons at various positions with respect to the neutral axis of the beam. Adaptive stiffening or morphing is activated via selective resistance heating of the SMA ribbons or uniform thermal loads on the beam. The thermomechanical behavior of these composites was simulated in ABAQUS using user-defined SMA elements. The examples demonstrate the usefulness of the methods for the design and simulation of SMA hybrid composites.

Keywords: shape memory alloys, Nitinol, ABAQUS, finite element analysis, post-buckling control, shape control, deflection control, adaptive stiffening, morphing, constitutive modeling, user element

1. INTRODUCTION

Shape memory alloys (SMAs) are a class of metals named for their ability to recover a particular shape in two unique ways. The “shape memory effect” allows the recovery of an inelastic deformation by heating and the “superelastic effect” allows the recovery upon load removal of a deformation that is larger than possible with only normal elasticity. These behaviors are enabled by a reversible thermoelastic phase transformation in the material that is controlled by temperature and stress levels [1, 2]. Austenite, the high symmetry parent phase which exists at high temperature, transforms to “twinned” or “self-accomodated” martensite, a low symmetry product phase, upon cooling with no applied load. Loading applied to either austenite or twinned martensite results in “oriented” or “detwinned” martensite with a macroscopic strain in the direction determined by the applied load. Heating martensite causes reverse transformation to austenite resulting in the recovery of any orientation strain. The temperatures at which the transformations occur at no load are generally referred to as M_f , M_s , A_s , A_f , where “M” and “A” are the phase and “f” and “s” refer to the “finish” and “start” temperatures for the given transformation.

SMAs are available in various forms: solid and porous bulk form, wire, ribbon, and thin film. The use of shape memory materials has extended to many fields with diverse applications such as medical devices, actuators, composites, structures and MEMS devices. There is a growing interest in

* cbrinson@northwestern.edu, phone 1-847-467-2347, fax 1-847-491-3915
<http://www.mech.northwestern.edu/dept/people/faculty/brinson.html>

the use of SMAs in adaptive materials and structures. The US government and its agencies have funded several research projects of this kind, including the DARPA Smart Wing Project, the NASA AVST Morphing Project, the Morphing Aircraft Structures (MAS) Program, the Smart Materials and Structures Demonstrations Program, and the Synthetic Multifunctional Materials (SMFM) Program. These projects investigate the use of SMAs to reduce drag, noise, vibration or acoustic signature, and to increase endurance, ballistic/blast protection and dynamic response.

A number of different types of adaptive SMA composites use SMA wires or ribbons embedded in a matrix. Matrix materials that have been used include polymers [3, 4], metals [5-7], plaster [8], and composites such as fiberglass-epoxy [9, 10] and carbon-epoxy [11]. Some applications use the SMA behavior to control the shape of the composite structure [12-14] or its vibrational [9, 15, 16] or buckling response [17, 18], while other applications use the SMA components to change the composite's stiffness [9, 19], to strengthen the composite [6], or to close or repair cracks [10, 20-22].

Several methods have been developed to study the thermomechanical response of SMA composites, including micromechanical methods [20, 23] and finite element analysis [17, 24, 25]. In some of these studies, special composite elements were created to study multi-layered composite plates [26-28] and layered beams [29]. In other studies, composite beams actuated by SMA wires or ribbons were modeled with separate matrix and SMA reinforcing members [24, 25]. In a recent finite element analysis of the buckling of a laminated composite shell, the SMA elements were modeled as 1-D wire elements, but reorientation of twinned martensite was not considered [17].

Extensive experimental and modeling work has also been conducted on active SMA polymer composites by Turner and his collaborators at NASA Langley Research Center [30-35]. Figure 1a shows a conceptual airplane with morphing airfoils made of a shape memory alloy hybrid composite and and Figure 1b shows a prototype adaptive stiffening beam at NASA in a temperature ramp test. In earlier work, Turner [36] developed the ECTE (effective coefficient of thermal expansion) model to describe the behavior of active SMA composites. This ECTE model requires only fundamental engineering properties such as stress and the Young's modulus for the particular conditions expected during the intended use (e.g., prestrain level and constraints). The model's predictions correlate very well with simple experimental data. However, the ECTE model does not take into account reorientation effects, cyclic loading, or partial loading and unloading and thus a more robust method to study the response of these composite beams and aid in design of the necessary materials properties, geometric placement of the ribbons and target temperature control strategies is needed.



Figure 1: Left) Conceptual airplane with morphing airfoil made of shape memory alloy hybrid composite; Right) Adaptive stiffening prototype beam at NASA undergoing a temperature ramp test [30].

This paper demonstrates and validates another approach in modeling active composites. We create a finite element model in ABAQUS using standard elements for the matrix (polymer composite) material and a user-defined element for the SMA reinforcing elements. This user element implements a rigorous 1-D shape memory alloy constitutive model. A 1-D SMA model is a reasonable approximation for these composites since the SMA components act mainly by a change in their lengths and non-uniaxial forces are relatively small. A brief discussion of 1-D models is given in the next section. Additional details are available in other papers [37, 38]. Several example problems are simulated and the results and implications are discussed.

2. CONSTITUTIVE MODEL AND FINITE ELEMENT IMPLEMENTATION

The SMA constitutive model used is based on a model originally formulated by Tanaka [39], and modified by Liang and Rogers [40] and subsequently by Brinson [41-43]. The one-dimensional model is based on phenomenological macro-scale constitutive behavior and can be written as

$$\sigma = E(\varepsilon - \varepsilon_L \xi_s) + \Theta \Delta T \quad (1)$$

where σ is stress and ε is strain; ξ_s is the stress-induced (oriented) martensite fraction, E is the elastic modulus, ε_L is the maximum transformation strain, and Θ is related to the thermal coefficient of expansion for the material.

Coupled to the constitutive law, a kinetic law must be used to determine the martensite volume fraction based on the stress and temperature loading history. The transformation criteria can be represented on an experimentally determined phase diagram shown in Figure 2. The kinetic law used in the simulations for this paper includes both twinned (self-accomodated) and detwinned (oriented) martensite variants [41], as is essential to properly handle the issue of martensitic variant reorientation. The kinetics are further enhanced to consider the full thermomechanical history implemented through “switching points” for changes in load path direction [43]. This allows the model to appropriately model hysteresis effects in the phase transformation and to capture cyclic or repetitive loading conditions, under which many kinetic laws fail. The reader is referred to the previous work for a full explanation and examples of the algorithms and only a brief synopsis is presented here for transformation between the [M] and [A] regions.

Whenever the thermomechanical state of the SMA material enters the shaded areas on the diagram of Figure 2, ξ_s must be updated. The thermomechanical path can be complex and the kinetic algorithm described here to update ξ_s is able to consistently reproduce the path dependence of martensitic transformation. Note in Figure 2 that the normal vectors \mathbf{n}_A and \mathbf{n}_M represent the directions of transformation change in the [A] and [M] strips respectively. At any point on the path, $\boldsymbol{\tau}$ is the vector tangent to Γ . A transformation occurs whenever one of the following conditions is satisfied:

$$\begin{aligned} \text{a) } & \boldsymbol{\tau} \cdot \mathbf{n}_A > 0 \text{ in [A]} \\ \text{b) } & \boldsymbol{\tau} \cdot \mathbf{n}_M > 0 \text{ in [M]} \end{aligned} \quad (2)$$

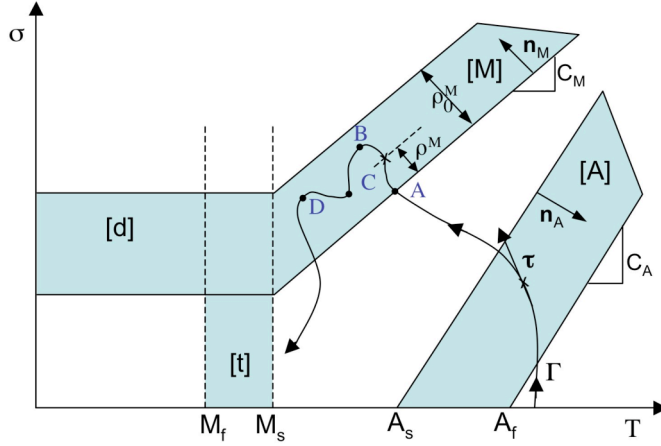


Figure 2: Typical phase diagram for a shape memory alloy. [M], [A], [d] and [t] are regions of transformation between martensite and austenite. [M] and [d] are associated with formation of detwinned martensite (with accompanying macroscopic strain), while [t] is associated with twinned martensite (no accompanying macroscopic strain). A thermomechanical loading path, Γ , is shown with several switching points indicated by solid circles. Loading path tangent, τ , and transformation strip distances, ρ , are indicated. At high σ and T , SMAs have a zone of irreversible plastic deformation which is not shown in this figure. The composite is loaded so that SMA wires do not enter this region as it is not useful for the applications considered in this paper.

A given loading path Γ can be subdivided into several segments ($\Gamma_n, n = 1, 2, \dots$) by introducing *switching points*, defined as the points where the direction or sense of the transformation changes. The switching points are points where Γ enters or leaves the transformation strip in the direction of transformation (point A) or points inside the strip where the dot product between τ and \mathbf{n}_A or \mathbf{n}_M changes sign (points B, C, D). Along the portions of Γ between two switching points, ξ_s is monotonically either increasing or decreasing (when in a transformation strip and moving in a transformation direction, e.g. between A and B or C and D) or constant (when outside a transformation strip or when moving opposite to the transformation direction, e.g. between B and C, or along any portions of Γ outside of the segment A to D).

Bekker and Brinson [43] present three ways to formulate the local kinetic law, one of which is utilized here. We first define $Y^i = Y^i(T, \sigma)$, ($i = A, M$) as the normalized distance between a given point on Γ inside a transformation strip and the start boundary. Y is given by the following expression

$$Y^i = \frac{\rho^i}{\rho_0^i}, \quad (3)$$

where ρ^i is the distance of point (T, σ) from the start boundary, and ρ_0^i is the width of the strip. Figure 2 illustrates these quantities for the case of the [M] strip.

On a given portion Γ_n between two switching points, ξ_s can then be updated using the appropriate one of the following expressions

$$\xi_s = \xi_s f^A(Y^A - Y_j^A) \quad (4)$$

when the point is inside the [A] strip, and

$$\xi_s = \xi_{sj} + (1 - \xi_{sj}) f^M(Y^M - Y_j^M) \quad (5)$$

when the point is inside the [M] strip.

In the forgoing expressions, quantities marked with subscript j are the values of the martensite fraction and the normalized distance at the previous switching point relevant to the current transformation, ξ_s is the stress-induced martensite fraction and f^j are interpolation functions. Here cosine interpolation functions are used, equivalent to those originally developed by Liang and Rogers [40]:

$$f^A(Y^A - Y_j^A) = 1 - \frac{1}{2}\{1 - \cos[\pi(Y^A - Y_j^A)]\} \quad (6)$$

$$f^M(Y^M - Y_j^M) = \frac{1}{2}\{1 - \cos[\pi(Y^M - Y_j^M)]\} \quad (7)$$

The Brinson model has been tested and found to be an excellent SMA model for modeling SMA wire reinforced composite structures [38, 44]. The kinetic and constitutive laws presented here have been implemented successfully for one-dimensional SMA response using the ABAQUS user element interface. The SMA user element includes a non-linear (both geometric and material) finite element procedure for the kinetic and constitutive laws, appropriate convergence criteria for both ABAQUS and the user element, tracking of converged and switching points while trying new predictions which may be rejected by ABAQUS. The readers are referred to [45] for more details. For the simulations presented in next section, the SMAs are modeled using the new SMA user element. The matrix is modeled using standard ABAQUS elements for laminated composite materials with temperature dependent material properties.

3. EXAMPLE PROBLEMS AND DISCUSSION

The composite beams consist of a matrix of laminated glass-epoxy layers reinforced with embedded shape memory alloy ribbons. The matrix is modeled using standard ABAQUS composite shell elements and the SMA ribbons are modeled with 1-D user-defined truss elements. Two examples are chosen to illustrate the applications of adaptive stiffening and shape control: thermal cycling of a beam clamped at both ends and a cantilevered beam with biased SMA reinforcements. Schematics of these two active control scenarios are illustrated in Figure 3. Non-linear static analyses of these composites are performed and compared to experimental results, providing insight into the capability of the simulation strategy and its usefulness as a design tool.

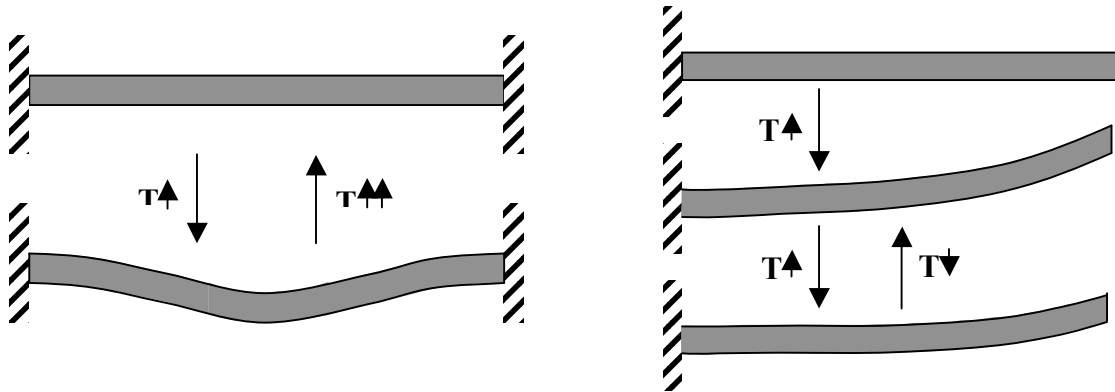


Figure 3: (Left) Schematic of clamped beam buckling, and (Right) Schematic of cantilever shape control

3.1. Clamped SMA hybrid composite beam

For easy comparison the beam specimen considered here is same as the one used by Turner and Patel [35] with slight modifications in the finite element model and mesh to render it suitable for analysis with the 1-D SMA user element. The experimental beam specimen is 18 inches long (45.72 cm) and 1 inch wide (2.54 cm) and clamped at both ends. The lamination stacking sequence is $(45/0/-45/90)_{2s}$ with SMA ribbon material replacing a width of 0.45 inches (1.143 cm) of the 0° glass-epoxy layers about the beam centerline, bounded by 0.275 inch (0.6985 cm) wide strips of glass-epoxy on either side. The thickness of each glass-epoxy layer is 0.004875 inches (0.012383 cm) and the thickness of the SMA ribbon is 0.006 inches (0.01524 cm). Thus, the prototype beam has a total thickness of 0.078 inch (0.19812 cm) at both edges and 0.0825 inch (0.20955 cm) in the center, and the beam cross-section is shown on the top plot of Figure 4. Since the SMA user element used is a truss it does not occupy a 2-D or 3-D space. The truss nature of the user element along with the symmetry of the four layers of ribbons and the loading allow the layers to be consolidated into a single user element row in the center of the beam. The implementation of the user elements uses the same total cross-sectional area as the total area of the four ribbon layers. Accordingly, the matrix layers in the center of the beam are modeled as 12 layers of glass-epoxy having a thickness of 0.0585 inch (0.14859 cm), as shown in the bottom plot of Figure 4. The SMA user elements and elements of the matrix are connected only by the common nodes along the center. This approximation decreases the moment of inertia of the beam and impacts the quantitative comparison of simulation and experimental results, as discussed later.

To develop the finite element mesh, the length of the beam is divided into 36 segments. ABAQUS allows laminated composite materials to be defined by the material and orientation stacking sequence. The matrix regions of both outer edges (16 layers of glass-epoxy) are modeled using $16 \times 36 \times 2$ S4 quadrilateral shell elements while the center (12 layers of glass-epoxy) is modeled with $12 \times 36 \times 2$ elements. The SMA ribbons are modeled with 36 truss elements sharing some common nodes with the $4 \times 36 \times 2$ shell elements on either side of the central line.

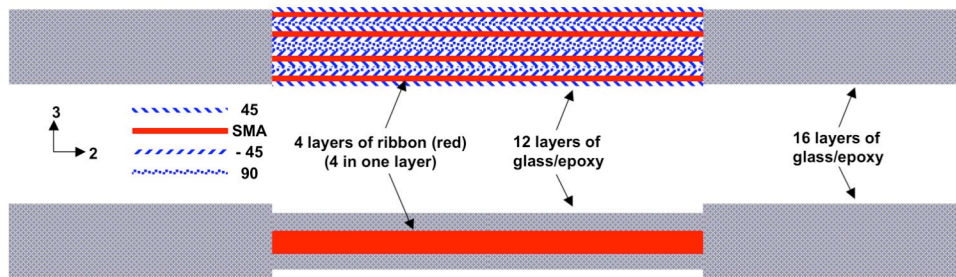


Figure 4: (Top) Schematic of the cross-section of the adaptive stiffening prototype beam and (Bottom) Finite element model

The properties used in this study for the SMA materials are listed in Table 1. Among these properties, the Young's modulus of austenite, the Poisson's ratio and density are same as those in [35], and the Young's modulus of martensite is set to half the modulus of austenite. The transformation temperatures are based on DSC test results in [32]. The phase diagram parameters and the maximum residual strain were not available for the SMA ribbon used in the composite and values were taken from [40, 46, 47] for a similar NiTi material. The thermal coefficient of thermal expansion for the NiTi ribbons is taken as zero for simplicity, as thermal strains alone are orders of

magnitude smaller than transformation strains. The properties for the glass-epoxy are same as in [35] and shown in Table 2 in the appendix.

Table 1. Material properties for the Nitinol alloy used in the simulations of adaptive stiffening and shape control composites

| Moduli, density | Transformation temperatures | Phase Diagram parameters | Max residual strain, Poisson's ratio |
|------------------------------------|------------------------------|--------------------------------------|--------------------------------------|
| $D_A = 3.94 \times 10^6$ psi | $M_f = 43.16^\circ\text{F}$ | $C_M = 644.4$ psi/ $^\circ\text{F}$ | $\epsilon_L = 0.067$ |
| $D_M = 1.97 \times 10^6$ psi | $M_s = 68.9^\circ\text{F}$ | $C_A = 1112$ psi/ $^\circ\text{F}$ | $\nu = 0.3$ |
| $\Theta = 0$ psi/ $^\circ\text{C}$ | $A_s = 128.48^\circ\text{F}$ | $\sigma_s^{\text{cr}} = 14500$ psi * | |
| $\rho = 0.2066$ lb/in ³ | $A_f = 142.34^\circ\text{F}$ | $\sigma_f^{\text{cr}} = 24650$ psi * | |

* critical stresses for multiple buckling examples: $\sigma_s^{\text{cr}} = 1000$ psi, $\sigma_f^{\text{cr}} = 10000$ psi

The ends of the model are clamped and the model is initially at 70°F (21.1°C). The model is loaded by applying a uniform temperature of 170°F (76.7°C). The model is cooled back to 70°F and is then reheated and re-cooled in several more thermal cycles for a total of five complete heating and cooling cycles. The combination of the thermal loads and the fixed boundary conditions causes thermoelastic instability and large thermal post-buckling deflections. To prevent numerical ill-conditioning, initial geometric imperfections were set as the deflections for a static gravity load of 1g (386.4 in/s², 9.81 m/s²), normal to the plane of the beam. These initial deflections were calculated in a separate static analysis.

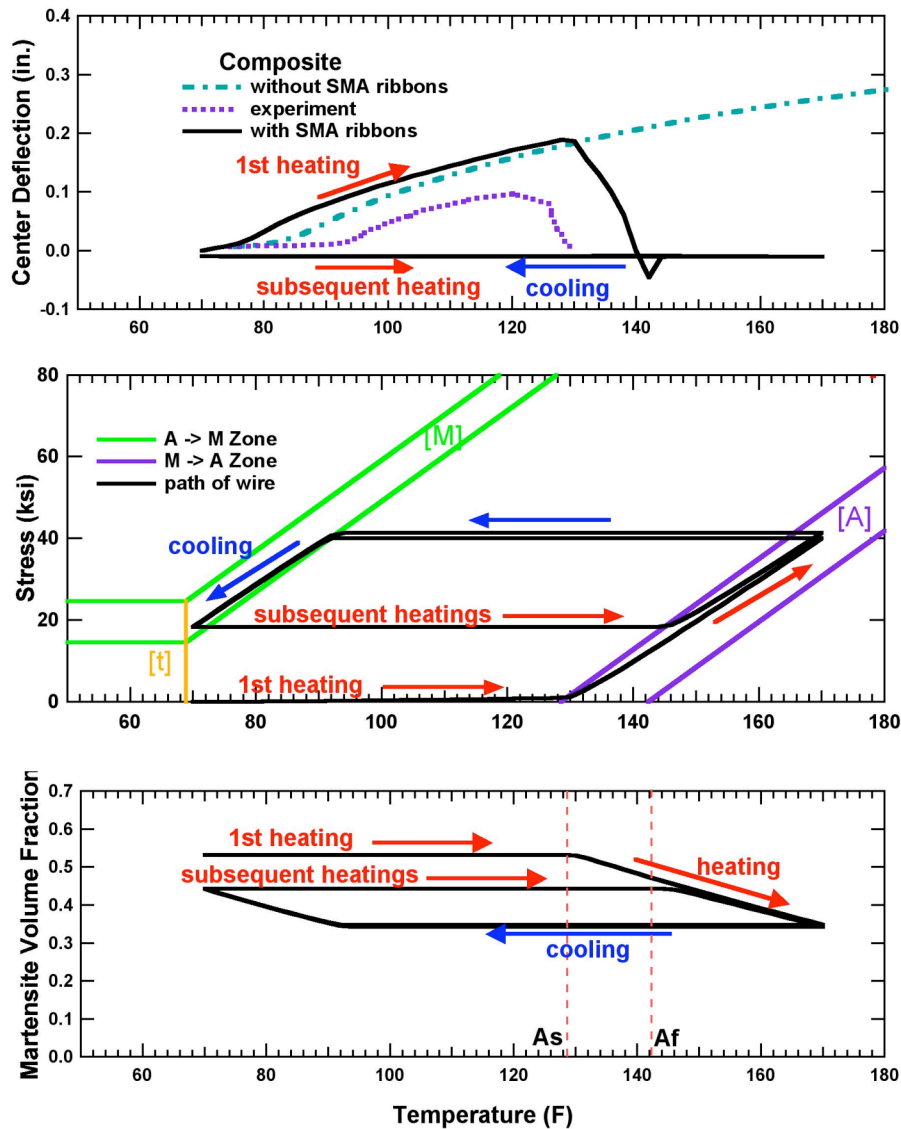


Figure 5: Buckling of heated adaptive stiffening composite. 5 complete heating and cooling cycles are plotted. (Top) Measured and predicted mid-span, post-buckling deflection, (Middle) Path in the phase diagram, (Bottom) Martensite volume fraction.

Figure 5 shows the change of several variables versus temperature including the measured and predicted mid-span, post-buckling deflection, the stress, and the martensite volume fraction of the shape memory elements. The mid-span, out-of-plane deflection versus temperature for the experimental measurement is also shown in the top plot of Figure 5 together with the simulation of a simple composite (no SMA ribbons), and simulation of the active SMA composite. For the simulation of the simple composite, the normal thermoelastic behavior causes a post-buckling deflection that increases with temperature, with a deflection of 0.26 inch at 167.4°F. For the active SMA composite, both the experimental result and the simulation show the normal thermoelastic buckling behavior up to certain temperature (approximately 130°F), at which point the SMA ribbons are actuated and begin to dominate the stress state. At higher temperatures, the structure is rendered

flat, even eliminating the initial imperfection deflection shown as an initial non-zero deflection. To enable this buckling control, the SMA ribbons must be embedded with some amount of detwinned martensite. The change in strain due to reverse transformation from detwinned martensite to austenite causes internal normal stresses to develop which reverse the buckling of the composite. This self-stiffening effect is activated for any temperature above the reverse transformation temperature of the SMA elements used. As the critical temperatures can be altered in SMAs with small changes in alloying elements and processing conditions, this adaptive stiffening effect can be tailored for specific applications so as to have a significant effect on the structure's dynamic response.

For the heating response, the simulation accurately captures the qualitative response of the experiment, however quantitative differences between the experimental data and the simulations remain. These differences may be due to several modeling approximations. The simulation assumes constant temperature throughout the specimen, while in the experiment the SMA ribbons are activated by resistive heating which is likely to cause a non-uniform temperature distribution. Differences between the SMA material properties used in the simulations and the SMA properties in the experiments are likely to account for other quantitative differences in the results: while some of the properties for the SMA were obtained by direct measurements of the ribbons, the phase diagram information was not available for the ribbons so parameters were used from a different material. As shown in the next simulation, small changes in SMA material properties can cause large changes in the behavior of the whole structure. The geometric approximations in which the center region is modeled as only 12 layers of simple composite material, reducing the moment of inertia, could also lead to delayed recovery in the simulation.

When the model is cooled, the beam remains flat due to the residual stresses in the SMA ribbons. These residual stresses in the ribbons also prevent subsequent rebuckling of the composite upon repeated heating cycles. This response is explained in the analysis of the other two plots. The middle and bottom plots of Figure 5 show the path of the shape memory element in the SMA phase diagram and the detwinned volume fraction versus temperature respectively. The SMA element starts from a zero stress state with some initial detwinned volume fraction corresponding to 3.5% prestrain. During heating, no significant changes in the stress or volume fraction occur until the temperature reaches A_s and the SMA element enters the reverse transformation zone [A]. At that point, the volume fraction begins to decrease linearly and the stress begins to increase due to the constraints on both ends of the beam. On the phase diagram, the SMA element does not cross completely through the [A] transformation zone, so the martensite volume fraction does not reduce to zero at the peak temperature of 170°F (76.7°C).

The structure is then cooled, but it does not rebuckle because the SMA ribbons transform back to martensite at a temperature that is lower than the temperature to transform to austenite. As further cooling moves the SMA into the zone for transformation to detwinned martensite [M], the resulting transformation reduces the stress (since detwinned martensite has a longer stress-free length than austenite). The reduction in stress moves the SMA downward through the zone, decreasing or preventing further transformation since only movement through the [M] zone in the direction from the right edge to the left edge of the zone causes transformation. As a result, the martensite volume

fraction at the end of the first cooling is somewhat lower than the initial value and the ribbons are left with a residual stress.

When the model is heated again, the residual stress in the ribbons is high enough to prevent buckling from occurring at any temperature as seen in the deflection plot. The stresses stay at the residual value until the model reaches the [A] transformation zone. Reverse transformation occurs as the temperature increases further and the stress increases accordingly due to the end constraints. The path in the [A] zone and subsequent cooling is only slightly different from the in those regions of the first heating and cooling. For additional heating and cooling cycles, the paths are identical to the second heating and cooling results. Similarly for the martensite volume fraction, once the reverse transformation begins, the results are similar to the first heating and cooling results. And for additional heating and cooling cycles, the martensite volume fraction varies exactly the same as for the second heating and cooling cycle.

Since buckling occurred only for the first heating cycle, the simulation does not model a typical application where it would be desirable for the shape control mechanism to work for multiple cycles. Buckling for the second heating is prevented by the relatively high residual stress. It is necessary to reduce that stress to allow the structure to buckle for subsequent heating. As mentioned earlier, the phase diagram data was not derived from measurements of the SMA ribbons used in the experiments, so those parameters are not exact. If the critical stress values are reduced, the resulting behavior can show multiple buckling deflections as seen in the top plot of Figure 6. In addition to the change of the SMA critical stresses (observed by comparing the phase diagram lines in the middle plots of Figures 5 and 6), the initial strain was decreased to 2.0%. The strain was reduced in part to compensate for the reduced critical stresses, but it was also reduced to lower the initial martensite volume fraction which in turn would lower the stress in the ribbons reached at the maximum temperature. Parameters used for the NiTi in the simulation in Figure 6 are given in Table 1 with alternate critical stresses given by “*” below the table.

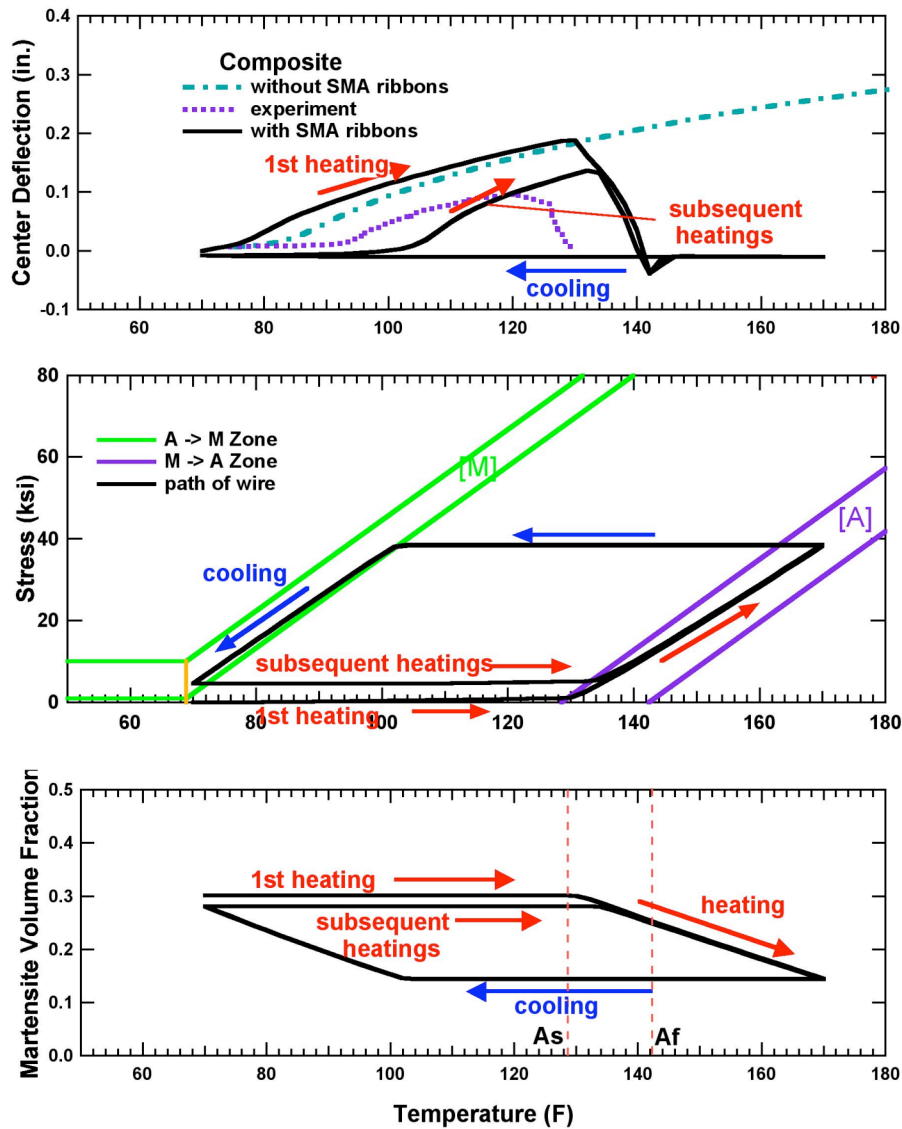


Figure 6: Adaptive stiffening composite with multiple buckling. All graphs plotted on same temperature scale.
 (Top) Measured and predicted mid-span, post-buckling deflection, (Middle) Path in the phase diagram,
 (Bottom) Martensite volume fraction.

The deflection plot shows that the beam does buckle for the second heating although at a higher temperature since there remains some residual stress in the ribbons after the first cooling. The buckling and flattening of the second and later heatings occur at higher temperatures and cause the maximum deflection to be smaller than for the first load cycle. After the first cooling, the residual stress is lower and the martensite volume fraction is closer to the initial volume fraction than in the previous simulation. The higher stress and lower martensite volume fraction at the beginning of the second and subsequent heatings cause the buckling to initiate at a higher temperature and to result in a lower maximum deflection compared to the response for the first heating. All the plots have identical results for all the cycles after the second cycle.

The significant change in response of the composite system due to relatively small changes in SMA material properties demonstrates the need for very careful determination of correct material properties to enable the desired system response. Additionally, the ability to simulate SMA composite behavior could be especially valuable for the design of SMA composite systems for shape control.

3.2. Cantilevered SMA hybrid composite beam

The second example demonstrates shape/deflection control of a cantilevered SMA hybrid composite beam. A cantilevered SMA hybrid composite beam is 9 inches long (22.86 cm) and 1 inch wide (2.54 cm) with one clamped end and the other end free. The cross section of the beam is same as the top schematic in Figure 3 except that the SMA ribbon material only replaces a width of 0.45 inch (1.143 cm) about the beam centerline in the 2nd 0° glass-epoxy layer as shown in the top schematic of Figure 7. Therefore, the prototype beam has a thickness of 0.078 inch (0.19812 cm) on both edges and 0.073125 inch (0.2009775 cm) in the center. As in the first example, in the finite element model the SMA ribbon is modeled as a user element row. For the cantilever, the composite is offset with respect to the nodes shared with the ribbons so that the ribbons are effectively at a position off the neutral axis of the beam. The SMA user elements are in the position of the 2nd 0° glass-epoxy layer and have the same cross-sectional area as the ribbon layer. The matrix in the center is modeled as 15 layers of glass-epoxy having a thickness of 0.073125 inch (0.1857375 cm), as shown in the bottom plot of Figure 7. Thus the section of beam containing the SMA ribbon is slightly thinner than in the prototype due to the missing layer that is replaced by the SMA ribbon.

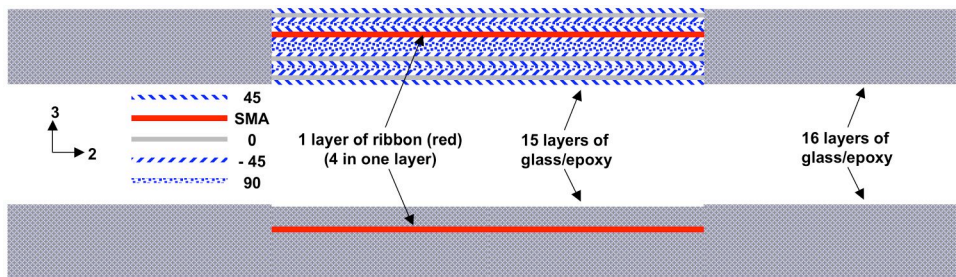


Figure 7: (Top) Schematic of the cross-section of the shape-control prototype beam and (Bottom) Finite element model.

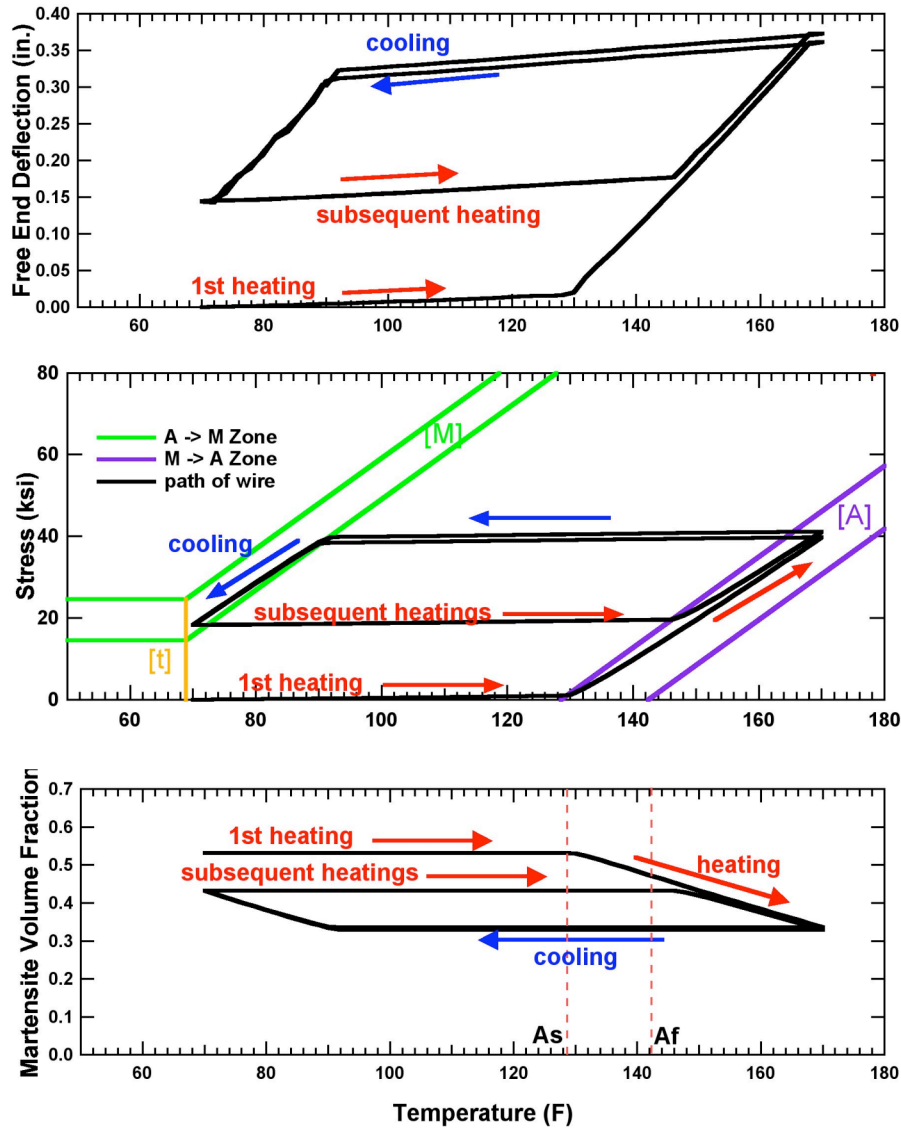


Figure 8: (Top) Predicted tip deflection versus temperature for the shape control composite; (Middle) Path in the phase diagram; (Bottom) Martensite volume fraction versus temperature of tip shape memory element.

The model was subjected to a uniformly distributed thermal load of 170°F (76.7°C) to study the deflection response. No perturbation of geometry was necessary in this case due to the non-symmetric location of the SMA ribbons off the neutral axis. The tip displacement of the beam is shown in the top plot of Figure 8. Before the SMA elements enter the reverse transformation zone [A] the tip displacement increases very slowly due to the different thermal expansion coefficients of the matrix and composite. Once in the zone, tip deflection increases rapidly with temperature due to a combined effect of shortening of SMA ribbons and expansion of the polymer composite. Upon cooling, before SMA elements enter the detwinning martensite zone [M] the tip deflection drops slowly with decreasing temperature due to the pure thermoelastic effect. In the transformation zone, tip deflection decreases rapidly with temperature. At room temperature, detwinned martensite remains as shown in the bottom plot of Figure 8 and therefore the stress in SMA elements is not

zero, which accounts for a small residual tip deflection of 0.174 inch (0.44149 cm). The large amount of change of tip displacement is clearly due to the reverse or forward transformation of SMA ribbons. This example demonstrates the effectiveness of SMA ribbons in shape control. The middle plot of Figure 8 shows the path of the tip SMA element in the phase diagram and the bottom plot of Figure 8 shows the martensite volume fraction versus temperature. These two plots are quite similar to those in the adaptive stiffening simulation. As in the previous example, the use of prestrained SMA ribbons is essential to achieve significant shape control. Although thermal coefficient of expansion mismatch between the SMA elements and the composite can account for some shape change, the magnitude is insignificant compared to the actuated tip deflections using prestrained SMA ribbons.

In Figure 7, the SMA ribbons replace the 2nd 0° glass-epoxy layer (16% offset) and one expects larger tip displacement if the SMA ribbons replace the 1st 0° glass-epoxy layer (41% offset). Figure 9 shows the linear relation between the tip deflection and the relative position of the shape memory ribbon layer in the composite beam. The above simulations demonstrate that finite element analysis is able to show the effects of adjusting design parameters such as the lowest and highest temperatures, the prestrain amount, the composite configuration, and the material properties of the matrix and SMA. Thus, it can be used to design composites that have desired shapes at specific temperatures. More control of the cantilever could be obtained by adding SMA ribbons on the opposite side of the neutral axis with independent heating and cooling of the two different SMA ribbon groups. This would enable the beam to be able to return to zero displacement as well as to bend in either direction, by differentially activating the two sets of ribbons. Such a simulation would require a true 3D analysis however in order to account for the placement of SMA ribbons at more than one location across the cross-section. The current analysis using shell elements for the beam allows only one ribbon location.

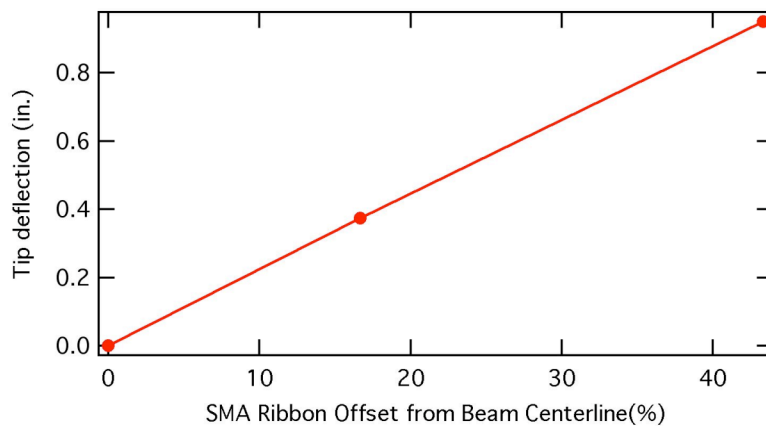


Figure 9: Tip deflection versus the relative position of the shape memory ribbon layer in the composite beam.

4. CONCLUSION

In this paper, simulations of adaptive stiffening and shape control of SMA hybrid composites have been demonstrated and compared to experimental results. A rigorous 1-D SMA model previously implemented using the ABAQUS user element interface has been used to simulate the 1-D response of the SMA reinforcements in such composites. The matrix of these composites is modeled using standard ABAQUS element types, including elements for laminated composite materials with temperature dependent material properties. Results of a non-linear static (post-buckling) analysis of a beam clamped at each end showed good correlation between experimental and simulation results. The deflection versus temperature response of a cantilevered beam demonstrated the efficient control authority of the embedded SMA. It can be concluded that SMAs are very good candidates for such composites and use of pre-strained SMA ribbons in these composites is critical.

An advantage of the simulation method developed here in which separate elements for the SMA reinforcements and matrix are used is that material properties or composite geometry can be changed easily. Other approaches in which special composite elements are developed which combine both SMA and matrix properties are more application specific. The flexibility and demonstrated robust performance in predicting adaptive stiffening and shape control behavior of the current approach allows the technique to be used to achieve optimal design and explore design issues for a composite, including material properties for matrix and SMA, prestrain amount and volume percentage of the SMA reinforcements, geometry arrangement, and working temperature range for the composite.

ACKNOWLEDGEMENT

Funding support from NASA-Langley is gratefully acknowledged.

REFERENCES

1. Funakubo, H., ed. *Shape Memory Alloys*. 1987, Gordon and Breach Science Publishers: New York.
2. Wayman, C.M. and T.W. Duerig, *An introduction to martensite and shape memory*, in *Engineering Aspects of Shape Memory Alloys*, T.W. Duerig, et al., Editors. 1990, Butterworth-Heinemann: Boston. p. 3-20.
3. Sittner, P., V. Michaud, and J. Schrooten, *Modelling and material design of SMA polymer composites*. *Materials Transactions*, 2002. **43**(5): p. 984-993.
4. Sun, S.S., et al., *Thermoviscoelastic analysis for a polymeric composite plate with embedded shape memory alloy wires*. *Composite Structures*, 2002. **58**(2): p. 295-302.
5. Armstrong, W.D., *A one-dimensional model of a shape memory alloy fiber reinforced aluminum metal matrix composite*. *Journal of Intelligent Material Systems and Structures*, 1996. **7**(4): p. 448-454.

6. Song, G.Q., Q.P. Sun, and M. Cherkaoui, *Role of microstructure in the thermomechanical behavior of SMA composites*. Journal of Engineering Materials and Technology-Transactions of the ASME, 1999. **121**(1): p. 86-92.
7. Yue, Z.F. and J.S. Wan, *Constitutive relationship and applications of shape-memory alloys*. Progress in Experimental and Computational Mechanics in Engineering, 2003. **243-2**: p. 487-491.
8. Watanabe, Y., E. Miyazaki, and H. Okada, *Enhanced mechanical properties of Fe-Mn-Si-Cr shape memory fiber/plaster smart composite*. Materials Transactions, 2002. **43**(5): p. 974-983.
9. Gupta, K., et al., *Stiffness characteristics of fibre-reinforced composite shaft embedded with shape memory alloy wires*. Defence Science Journal, 2003. **53**(2): p. 167-173.
10. Hamada, K., F. Kawano, and K. Asaoka, *Shape recovery of shape memory alloy fiber embedded resin matrix smart composite after crack repair*. Dental Materials Journal, 2003. **22**(2): p. 160-167.
11. Lee, H.J., J.J. Lee, and J.S. Huh, *A simulation study on the thermal buckling behavior of laminated composite shells with embedded shape memory alloy (SMA) wires*. Composite Structures, 1999. **47**(1-4): p. 463-469.
12. Brinson, L.C., et al., *Analysis of controlled beam deflections using SMA wires*. Journal of Intelligent Material Systems and Structures, 1997. **8**(1): p. 12-25.
13. Lind, R.J. and C.C. Doumanidis, *Active deformable sheets: prototype implementation, modeling, and control*. Optical Engineering, 2003. **42**(2): p. 304-316.
14. Oh, J.T., H.C. Park, and W. Hwang, *Active shape control of a double-plate structures using piezoceramics and SMA wires*. Smart Materials & Structures, 2001. **10**(5): p. 1100-1106.
15. Aoki, T. and A. Shimamoto, *Active vibration control of epoxy matrix composite beams with embedded shape memory alloy TiNi fibers*. International Journal of Modern Physics B, 2003. **17**(8-9): p. 1744-1749.
16. Brinson, L.C. and R. Lammering, *Finite-Element Analysis of the Behavior of Shape-Memory Alloys and Their Applications*. International Journal of Solids and Structures, 1993. **30**(23): p. 3261-3280.
17. Lee, H.J. and J.J. Lee, *A numerical analysis of the buckling and postbuckling behavior of laminated composite shells with embedded shape memory alloy wire actuators*. Smart Materials & Structures, 2000. **9**(6): p. 780-787.
18. Birman, V., *Theory and comparison of the effect of composite and shape memory alloy stiffeners on stability of composite shells and plates*. International Journal of Mechanical Sciences, 1997. **39**(10): p. 1139-1149.
19. Boyd, J.G. and D.C. Lagoudas, *Thermomechanical Response of Shape-Memory Composites*. Journal of Intelligent Material Systems and Structures, 1994. **5**(3): p. 333-346.
20. Araki, S., H. Ono, and K. Saito, *Micromechanical analysis of crack closure mechanism for intelligent material containing TiNi fibers - (1st report, modeling of crack closure mechanism*

and analysis of stress intensity factor). JSME International Journal Series A-Solid Mechanics and Material Engineering, 2002. **45**(2): p. 208-216.

21. Shimamoto, A., et al., *Effect of crack closure by shrinkage of embedded shape-memory TiNi fiber epoxy composite under mixed-mode loading*. International Journal of Materials & Product Technology, 2001: p. 263-268.
22. Wang, X.M., *Shape memory alloy volume fraction of pre-stretched shape memory alloy wire-reinforced composites for structural damage repair*. Smart Materials & Structures, 2002. **11**(4): p. 590-595.
23. Kawai, M., et al., *Micromechanical analysis for hysteretic behavior of unidirectional TiNiSMA fiber composites*. Journal of Intelligent Material Systems and Structures, 1999. **10**(1): p. 14-28.
24. Ghomshei, M.M., et al., *Finite element modeling of shape memory alloy composite actuators: Theory and experiment*. Journal of Intelligent Material Systems and Structures, 2001. **12**(11): p. 761-773.
25. Sun, S.S., G. Sun, and J.S. Wu, *Thermo-viscoelastic bending analysis of a shape memory alloy hybrid epoxy beam*. Smart Materials & Structures, 2002. **11**(6): p. 970-975.
26. Zak, A.J., M.P. Cartmell, and W. Ostachowicz, *Dynamics of multilayered composite plates with shape memory alloy wires*. Journal of Applied Mechanics-Transactions of the ASME, 2003. **70**(3): p. 313-327.
27. Ostachowicz, W., M. Krawczuk, and A. Zak, *Natural frequencies of multi-layer composite plate with embedded shape memory alloy wires*. Journal of Intelligent Material Systems and Structures, 1998. **9**(3): p. 232-237.
28. Lagoudas, D.C., et al., *Modeling of the thermomechanical response of active laminates with SMA strips using the layerwise finite element method*. Journal of Intelligent Material Systems and Structures, 1997. **8**(6): p. 476-488.
29. Marfia, S., E. Sacco, and J.N. Reddy, *Superelastic and shape memory effects in laminated shape-memory-alloy beams*. AIAA Journal, 2003. **41**(1): p. 100-109.
30. Turner, T.L., C.L. Lach, and R.J. Cano. *Fabrication and characterization of SMA hybrid composites*. in *Smart Structures and Materials 2001-Active Materials; Behavior and Mechanics*. 2001. Newport Beach, CA: Society of Photo-Optical Instrumentation Engineers.
31. Turner, T.L. *Dynamic response tuning of composite beams by embedded shape memory alloy actuators*. in *Smart Structures and Materials 2000 - Industrial and Commercial Applications of Smart Structures Technologies*. 2000. Newport Beach, CA, USA: Society of Photo-Optical Instrumentation Engineers, Bellingham, WA, USA.
32. Lach, C.L., et al. *Effects of thermomechanical history on the tensile behavior of Nitinol ribbon*. in *Smart Structures and Materials: Active Materials: Behavior and Mechanics*. 2002. San Diego, CA, United States: The International Society for Optical Engineering.
33. Turner, T.L. *Structural acoustic response of a shape memory alloy hybrid composite panel (lessons learned)*. in *Smart Structures and Materials 2002: Smart Structures and Integrated Systems*. 2002. San Diego, CA, United States: The International Society for Optical Engineering.

34. Turner, T.L., et al. *Design, fabrication, and testing of SMA enabled adaptive chevrons for jet noise reduction*. in *Smart Structures and Materials 2004 - Smart Structures and Integrated Systems*. 2004. San Diego, CA, United States: International Society for Optical Engineering, Bellingham, WA 98227-0010, United States.
35. Turner, T.L. and H.D. Patel. *Analysis of SMA hybrid composite structures using commercial codes*. in *Smart Structures and Materials 2004 - Modeling, Signal Processing, and Control*. 2004. San Diego, CA, United States: International Society for Optical Engineering, Bellingham, WA 98227-0010, United States.
36. Turner, T.L., *A new thermoelastic model for analysis of shape memory alloy hybrid composites*. *J. Intell. Mater. Syst. Struct.*, 2000. **11**(5): p. 382-394.
37. Gao, X., D.S. Burton, and L.C. Brinson, *Finite element simulation of a self-healing shape memory alloy composite*. *Mech. Mater.*, 2005. **in press**.
38. Zak, A.J., et al., *One-dimensional shape memory alloy models for use with reinforced composite structures*. *Smart Materials & Structures*, 2003. **12**(3): p. 338-346.
39. Tanaka, K., S. Kobayashi, and Y. Sato, *Thermomechanics of Transformation Pseudoelasticity and Shape Memory Effect in Alloys*. *International Journal of Plasticity*, 1986. **2**(1): p. 59-72.
40. Liang, C. and C.A. Rogers, *One-Dimensional Thermomechanical Constitutive Relations for Shape Memory Materials*. *Journal of Intelligent Material Systems and Structures*, 1990. **1**(2): p. 207-234.
41. Brinson, L.C., *One Dimensional Constitutive Behavior of Shape Memory Alloys: thermomechanical derivation with non-constant material functions*. *Journal of Intelligent Material Systems and Structures*, 1993. **4**(2): p. 229-242.
42. Brinson, L.C. and M.S. Huang, *Simplifications and comparisons of shape memory alloy constitutive models*. *Journal of Intelligent Material Systems and Structures*, 1996. **7**(1): p. 108-114.
43. Bekker, A. and L.C. Brinson, *Phase diagram based description of the hysteresis behavior of shape memory alloys*. *Acta Materialia*, 1998. **46**(10): p. 3649-3665.
44. Prahlad, H. and I. Chopra, *Comparative evaluation of shape memory alloy constitutive models with experimental data*. *Journal of Intelligent Material Systems and Structures*, 2001. **12**(6): p. 383-395.
45. Gao, X., Qiao, R. and L.C. Brinson, *Implementation of a 1D phase-diagram based SMA model using ABAQUS' user element interface while considering orientation, prestrain and compression*. manuscript in preparation, 2005.
46. Liang, C., *The constitutive modeling of shape memory alloys*. 1990, Virginia Polytechnic Institute and State University: Blacksburg, VA.
47. Dye, T.E., *An experimental investigation of the behavior of nitinol*. 1990, Virginia Polytechnic Institute and State University: Blacksburg, VA.

APPENDIX

Table 2. Properties for the glass-epoxy matrix

(Coefficient of thermal expansion is relative to 75°F and mass density is 0.07338 lb/in³)

| T (°F) | E ₁ (psi) | E ₂ (psi) | ν ₁₂ | G ₁₂ (psi) | G ₁₃ (psi) | G ₂₃ (psi) | a ₁ (1/°F) | a ₂ (1/°F) |
|--------|----------------------|----------------------|-----------------|-----------------------|-----------------------|-----------------------|-----------------------|-----------------------|
| 60 | 7.15E+06 | 2.90E+06 | 0.29 | 1.40E+06 | 1.40E+06 | 1.40E+06 | 2.928E-06 | 6.139E-06 |
| 70 | 7.15E+06 | 2.90E+06 | 0.29 | 1.40E+06 | 1.40E+06 | 1.40E+06 | 2.985E-06 | 6.417E-06 |
| 80 | 7.15E+06 | 2.90E+06 | 0.29 | 1.40E+06 | 1.40E+06 | 1.40E+06 | 3.155E-06 | 7.253E-06 |
| 100 | 7.13E+06 | 2.82E+06 | 0.29 | 1.34E+06 | 1.34E+06 | 1.34E+06 | 3.471E-06 | 9.190E-06 |
| 120 | 7.11E+06 | 2.75E+06 | 0.29 | 1.29E+06 | 1.29E+06 | 1.29E+06 | 3.677E-06 | 1.068E-05 |
| 140 | 7.08E+06 | 2.68E+06 | 0.29 | 1.24E+06 | 1.24E+06 | 1.24E+06 | 3.761E-06 | 1.157E-05 |
| 150 | 7.07E+06 | 2.64E+06 | 0.29 | 1.22E+06 | 1.22E+06 | 1.22E+06 | 3.771E-06 | 1.184E-05 |
| 160 | 7.07E+06 | 2.58E+06 | 0.29 | 1.20E+06 | 1.20E+06 | 1.20E+06 | 3.766E-06 | 1.202E-05 |
| 180 | 7.06E+06 | 2.47E+06 | 0.29 | 1.15E+06 | 1.15E+06 | 1.15E+06 | 3.735E-06 | 1.220E-05 |
| 200 | 7.05E+06 | 2.35E+06 | 0.29 | 1.10E+06 | 1.10E+06 | 1.10E+06 | 3.696E-06 | 1.224E-05 |
| 220 | 7.05E+06 | 2.22E+06 | 0.29 | 9.80E+05 | 9.80E+05 | 9.80E+05 | 3.671E-06 | 1.223E-05 |
| 240 | 7.04E+06 | 2.09E+06 | 0.29 | 8.70E+05 | 8.70E+05 | 8.70E+05 | 3.669E-06 | 1.225E-05 |
| 250 | 7.04E+06 | 2.03E+06 | 0.29 | 8.10E+05 | 8.10E+05 | 8.10E+05 | 3.677E-06 | 1.228E-05 |
| 260 | 7.05E+06 | 1.95E+06 | 0.29 | 7.50E+05 | 7.50E+05 | 7.50E+05 | 3.691E-06 | 1.233E-05 |
| 280 | 7.06E+06 | 1.80E+06 | 0.29 | 6.20E+05 | 6.20E+05 | 6.20E+05 | 3.726E-06 | 1.247E-05 |
| 300 | 7.08E+06 | 1.65E+06 | 0.29 | 5.00E+05 | 5.00E+05 | 5.00E+05 | 3.767E-06 | 1.264E-05 |